Mitigating Voltage Fluctuations in Battery Energy Storage Systems

Roosa-Maria Sallinen
Faculty of Information Technology and Communication Sciences
Tampere University
Tampere, Finland
roosa.sallinen@tuni.fi

Tuomas Messo
Faculty of Information Technology and Communication Sciences
Tampere University
Tampere, Finland
tuomas.messo@tuni.fi

Tomi Roinila
Faculty of Engineering and Natural Sciences
Tampere University
Tampere, Finland
tomi.roinila@tuni.fi

***Abstract*—Battery Energy Storage Systems (BESSs) play an important role in grid-connected renewable energy systems as they provide great flexibility in the energy production. For photovoltaic (PV) energy applications, the BESS may be connected to the dc-link of the converter system to inject the deficit or to absorb the surplus of generated power. One of the main issues in such systems is the voltage variation at the dc-link, especially under grid imbalance, distorting the current fed to the grid. This paper studies a method to control the BESS to emulate a capacitance, thus mitigating the dc-link voltage fluctuation, for example, under heavy imbalance.**

***Index Terms*—Battery energy storage system, dc-link voltage fluctuation, virtual capacitance, PV-inverter, imbalance**

I. Introduction

Battery energy storage systems (BESSs) are gaining popularity as a supplement to grid-connected photovoltaic (PV) generators as they enable using the energy when needed instead of when generated [1]. BESSs have several applications in power systems, such as peak load shaving, power outage mitigation, and frequency regulation [2], [3]. However, regardless of the advancements made in the field, they are still fairly expensive components and often have a relatively short lifespan [4]. Therefore, it should be a priority to utilize BESSs as efficiently as possible.

In PV applications, a BESS is often connected to the dc-link of an inverter that functions as the system's grid interface. In such a system, the dc-link voltage regulation is important in order to guarantee that the current fed to the grid complies with the grid codes. To this end, commonly a large capacitor per unit volume is placed on the dc-link to mitigate the voltage fluctuations. The capacitor also limits the dc-link voltage ripple, absorbs harmonics, and provides energy storage during transients [5]. However, a large capacitor increases the total cost and size of the system as well as slows down the voltage response during start-up phase [6].

To overcome these drawbacks, recent studies have proposed methods that enable the use of reduced dc-link capacitors in inverter-based systems without losing system reliability [6], [7]. The work in [6] presented an estimator-based method for a motor-drive application that stabilizes both the dc-link voltage and the motor current so that a reduced dc-link capacitor may be used. The work in [7] proposed an active power compensator in order to remove the second harmonic ripple of the dc-link voltage under imbalanced grid-voltages. However, applications involving a BESS have not been considered in these previous studies.

In order to attenuate the dc-link voltage variations in a grid-connected BESS with a reduced capacitor, a feedback/feedforward control strategy has been proposed [8]. This approach is based on the assumption that the BESS (instead of the inverter) controls the dc-link voltage. However, this may not always be the case, e.g., in PV applications [9]. For such a system, in which the inverter controls the dc-link voltage, the work in [10] proposed a method to emulate a BESS as a capacitor in order to synthesize extra inertia. However, as the main focus of the work in [10] is to compare dc-link capacitance with system inertia and to synthesize extra inertia to the system, it does not include a further analysis of the system dynamics nor address the control in the frequency-domain.

This paper analyses the method of controlling a BESS to emulate a (virtual) capacitance. The analysis is performed using small-signal models to enable reliable and straightforward investigation of the system dynamics and control design. The limitations and possible issues of the control algorithm are also emphasized. As a result, the system dynamics can be adjusted by using this controllable virtual capacitance. Special focus is given on the application where a BESS is connected to a dc-link. In this case, the BESS effectively increases the dc-link capacitance, thus, for example, mitigating the second order harmonic in the dc-link voltage during a grid imbalance. The analysis is confirmed by simulations both in the time and frequency domain.

The remainder of the paper is organized as follows. In Section II, the basic idea and analysis behind the capacitance emulation algorithm are presented. In Section III, the required small-signal models are derived. That is, the dynamics of the battery charger emulating a capacitance are determined. Section IV demonstrates and further analyses the ability of the control algorithm to affect the system dynamics and to mitigate

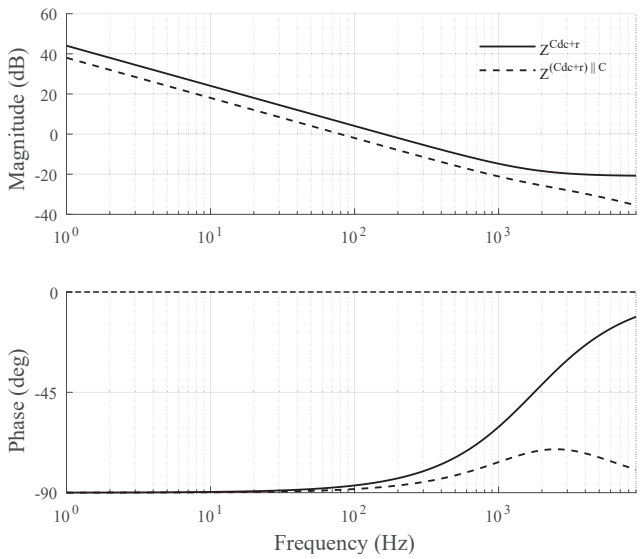

Fig. 1. The impedances of an RC circuit (solid line) and an RC circuit in parallel with a capacitor (dashed line).

the dc-link voltage fluctuation. The paper is summarized in Section V.

II. Capacitance Emulation

The impedance of a dc-link capacitor is generally given as

$$Z^{\text{Cdc+r}} = r_{\text{Cdc}} + \frac{1}{C_{\text{dc}}s}, \tag{1}$$

where C_{dc} is the (dc-link) capacitance and r_{Cdc} its parasitic resistance. When connecting the dc-link capacitor in parallel with an ideal capacitor (that is, the parasitic resistance is ignored), their total impedance can be presented as

$$Z^{(\text{Cdc+r})\|\text{C}} = \frac{1 + r_{\text{Cdc}}C_{\text{dc}}s}{r_{\text{Cdc}}C_{\text{dc}}Cs^2 + (C_{\text{dc}} + C)\,s}, \tag{2}$$

where C is the ideal capacitance. Fig. 1 gives an example where the impedances given by (1) and (2) are shown (the parameter values are specified in Table I). The addition of the capacitor in parallel lowers the magnitude of the impedance, hence mitigating variations/disturbances in the voltage more effectively.

In order to control the BESS to emulate a capacitance (in terms of impedance), the battery charger needs to control its output current i_{o}^{bc} according to

$$i_{\text{o}}^{\text{bc-ref}} \;=\; -C_{\text{em}}\frac{dv_{\text{o}}^{\text{bc}}}{dt} \;=\; -C_{\text{em}}sv_{\text{o}}^{\text{bc}}, \tag{3}$$

where C_{em} represents the emulated capacitance and v_{o}^{bc} the output voltage of the battery charger. Note that here the positive direction of the current is defined as out of the battery charger. As impedance/admittance is (by definition) measured when the current goes into the device, it requires a minus sign.

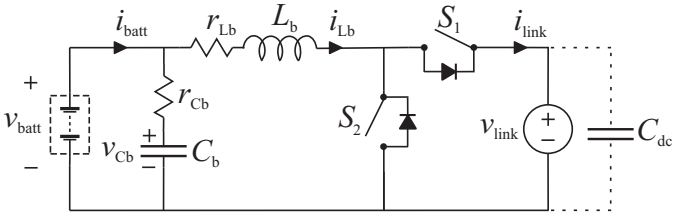

Fig. 2. Bi-directional dc-dc converter used as battery charger.

With this control, the output impedance of the BESS would ideally become

$$Z_{\text{C-em}} = \frac{1}{C_{\text{em}}s}. \tag{4}$$

A similar control principle has been used, e.g., in [10].

Using the Euler discretization method, the control algorithm (3) can be presented in discrete-time as

$$i_{\text{o}}^{\text{bc-ref}}(z) \;=\; -C_{\text{em}}\frac{z-1}{T_{\text{s}}}v_{\text{o}}^{\text{bc}}, \tag{5}$$

where T_{s} is the sampling interval.

It is emphasized, that any controller that utilizes numerical derivative is sensitive to noise. The sensitivity is inversely proportional to the magnitude of the sampling time [11]. Hence, in a practical system, a low-pass filter should be used to filter out the noise. Otherwise the output of the controller may fluctuate severely, possibly decreasing the lifetime of the switches.

III. Small-Signal Model of the Battery Charger for Capacitance Emulation

Fig. 2 presents a schematic diagram of a bi-directional dc-dc converter in which the output current i_{link} is defined as an output variable. That is, the dc-link can be modelled as a constant voltage source. Note that the direction of the current is as in discharging mode and, in this paper, will be defined as the positive current direction. In charging mode, the flow is the opposite and the current is defined as negative.

In order to derive a small-signal model for the system, the state vector, and input and output vectors are defined as

$$\hat{\mathbf{x}}(t) = \begin{bmatrix} \hat{v}_{\text{Cb}}^{\text{bc}} \\ \hat{i}_{\text{Lb}}^{\text{bc}} \end{bmatrix}, \hat{\mathbf{u}}(t) = \begin{bmatrix} \hat{v}_{\text{batt}}^{\text{bc}} \\ \hat{v}_{\text{link}}^{\text{bc}} \\ \hat{d}^{\text{bc}} \end{bmatrix}, \hat{\mathbf{y}}(t) = \begin{bmatrix} \hat{i}_{\text{batt}}^{\text{bc}} \\ \hat{i}_{\text{link}}^{\text{bc}} \end{bmatrix}, \tag{6}$$

respectively. Note that switch S_2 is controlled by duty cycle d^{bc} and switch S_1 by its opposite, $1-d^{\text{bc}}$. The linearised state-space representation of the battery charger can be given as,

$$\frac{d\hat{\mathbf{x}}(t)}{dt} = \mathbf{A}\hat{\mathbf{x}}(t) + \mathbf{B}\hat{\mathbf{u}}(t) \tag{7}$$

$$\hat{\mathbf{y}}(t) = \mathbf{C}\hat{\mathbf{x}}(t) + \mathbf{D}\hat{\mathbf{u}}(t), \tag{8}$$

where the state, input, output, and feed-through matrices $\mathbf{A}$, $\mathbf{B}$, $\mathbf{C}$, and $\mathbf{D}$, respectively, are given in the Appendix.

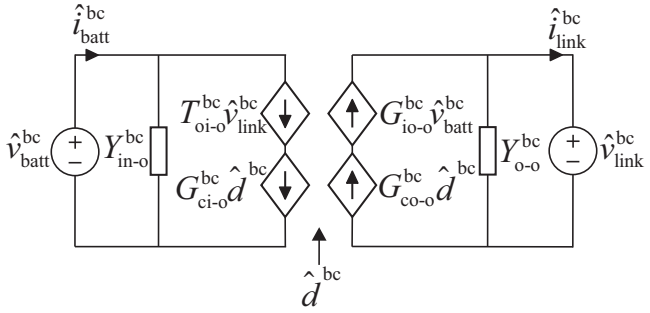

Fig. 3. Linear equivalent model of the bi-directional dc-dc converter used as battery charger.

The transfer functions from the input variables to the output variables at open loop can be solved in the s-domain by noting that

$$\mathbf{y}(s) = \Big(\mathbf{C}(s\mathbf{I} - \mathbf{A})^{-1}\mathbf{B} + \mathbf{D}\Big)\,\mathbf{u}(s), \tag{9}$$

where $\mathbf{I}$ is the identity matrix [12]. As a result, the open-loop dynamics can be presented in matrix-form as

$$\begin{bmatrix} \hat{i}^{\text{bc}}_{\text{batt}} \\ \hat{i}^{\text{bc}}_{\text{link}} \end{bmatrix} = \begin{bmatrix} Y^{\text{bc}}_{\text{in-o}} & T^{\text{bc}}_{\text{oi-o}} & G^{\text{bc}}_{\text{ci-o}} \\ G^{\text{bc}}_{\text{io-o}} & -Y^{\text{bc}}_{\text{o-o}} & G^{\text{bc}}_{\text{co-o}} \end{bmatrix} \begin{bmatrix} \hat{v}^{\text{bc}}_{\text{batt}} \\ \hat{v}^{\text{bc}}_{\text{link}} \\ \hat{d}^{\text{bc}} \end{bmatrix} \tag{10}$$

where the 2x3 matrix consists of the transfer functions between the input and the output variables. Fig. 3 illustrates the linear equivalent model of the system. The change in the converter transient response caused by a load change can be directly seen from the output impedance $Y^{\text{bc}}_{\text{o-o}}$ (when controlled in open-loop).

By utilizing a feedback controller on the battery charger output current according to the capacitance emulation algorithm given in (3), the closed-loop dynamics can be presented as

$$\begin{aligned} \begin{bmatrix} \hat{i}^{\text{bc}}_{\text{batt}} \\ \hat{i}^{\text{bc}}_{\text{link}} \end{bmatrix} &= \begin{bmatrix} Y^{\text{bc-Cem}}_{\text{in-c}} & T^{\text{bc-Cem}}_{\text{oi-c}} \\ G^{\text{bc-Cem}}_{\text{io-c}} & -Y^{\text{bc-Cem}}_{\text{o-c}} \end{bmatrix} \overbrace{\begin{bmatrix} \hat{v}^{\text{bc}}_{\text{batt}} \\ \hat{v}^{\text{bc}}_{\text{link}} \end{bmatrix}}^{\hat{\mathbf{u}}_{\text{Cem.}}} \\ &= \begin{bmatrix} Y^{\text{bc}}_{\text{in-o}} - \dfrac{G^{\text{bc}}_{\text{PI}} G^{\text{bc}}_{\text{ci-o}} G^{\text{bc}}_{\text{io-o}}}{1 + L_{\text{out-bc}}} & T^{\text{bc}}_{\text{oi-o}} + \dfrac{G^{\text{bc}}_{\text{PI}} G^{\text{bc}}_{\text{ci-o}} Y^{\text{S}}_{\text{o}}}{1 + L_{\text{out-bc}}} \\ G^{\text{bc}}_{\text{io-o}} - \dfrac{G^{\text{bc}}_{\text{PI}} G^{\text{bc}}_{\text{co-o}} G^{\text{bc}}_{\text{io-o}}}{1 + L_{\text{out-bc}}} & -Y^{\text{bc}}_{\text{o-o}} + \dfrac{G^{\text{bc}}_{\text{PI}} G^{\text{bc}}_{\text{co-o}} Y^{\text{S}}_{\text{o}}}{1 + L_{\text{out-bc}}} \end{bmatrix} \hat{\mathbf{u}}_{\text{Cem.}}, \end{aligned} \tag{11}$$

where

$$Y^{\text{S}}_{\text{o}} = Y^{\text{bc}}_{\text{o-o}} - C_{\text{em}} s, \tag{12}$$

$$L_{\text{out-bc}} = G^{\text{bc}}_{\text{PI}} G^{\text{bc}}_{\text{co-o}}, \tag{13}$$

in which a proportional-integral (PI) controller $G^{\text{bc}}_{\text{PI}}$ is used to regulate the output current. Assuming $L_{\text{out-bc}} \gg 1$ (i.e. within the control bandwidth), the closed loop output admittance $Y^{\text{bc-Cem}}_{\text{o-c}}$ becomes equal to $-C_{\text{em}}s$, i.e. the output impedance of a capacitance (the inverse of (4)). Fig. 4 illustrates the (discretized) control structure.

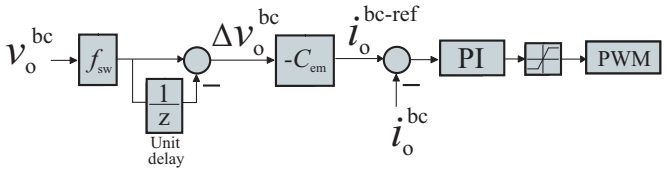

Fig. 4. Control block diagram of the battery controller for capacitor emulation.

TABLE I
PARAMETERS USED IN THE SIMULATION RESULTS

DC-DC converter		
Parameter	***Symbol***	***Value***
dc-link voltage	V_{link}	480 V
battery terminal voltage	V_{batt}	200 V
dc-link capacitance	C_{dc}	1 mF
parasitic resistance of dc-link capacitance	r_{Cdc}	90 mΩ
additional dc-link capacitance	C	1 mF
emulated dc-link capacitance	C_{em}	1 mF
switching frequency	f_{sw}	20 kHz
battery-side capacitor	C_{b}	1 μF
battery-side inductor	L_{b}	1.3 mH
PV inverter		
Parameter	***Symbol***	***Value***
MPP conditions (STC)	$V_{\text{pv-mpp}}$, $I_{\text{pv-mpp}}$	480 V, 8 A
grid voltage (RMS)	$V_{\text{a,b,c}}$	240 V
grid frequency	f_{g}	60 Hz
L-filter	L	1 mH

It may be obvious, that a safe use of a battery must be guaranteed, for example, by saturation limits. The controller should be implemented to limit the current and voltage at the battery terminal to avoid extensive stress on the battery. However, for simplicity and clarity, the implementation of this has been left out in this paper. That is, the focus is only on the capacitor emulation. Furthermore, in a real application, the control function would mainly be used as a supplementary control algorithm.

IV. Analysis and Simulation Results

This section demonstrates and further analyses the ability of the control algorithm to mitigate the dc-link voltage fluctuation. First, analysis and simulations regarding only the battery charger shown in Fig. 2 are given. After this, a more practical case is considered where the battery system is connected to a PV inverter.

The parameters used in the simulations are specified in Table I. The crossover frequency of the PI-controller is chosen as 800 Hz since higher value would decrease the phase margin to <65° due to control delay. The controller zero is located to have -135° minimum phase at low frequencies. The system control to output transfer function $G^{\text{bc}}_{\text{co-o}}$ as well as the resulting control loop gain $L_{\text{out-bc}}$ are shown in Fig. 5.

Fig. 6 presents the frequency response of the total output impedance Z_{o} for three different cases. In the first case (dashed green line), only the output impedance of the dc-link capacitor (i.e. 90 mΩ, 1 mF) was considered (without the BESS). In the second case (dashed blue line), an additional capacitor (1 mF)

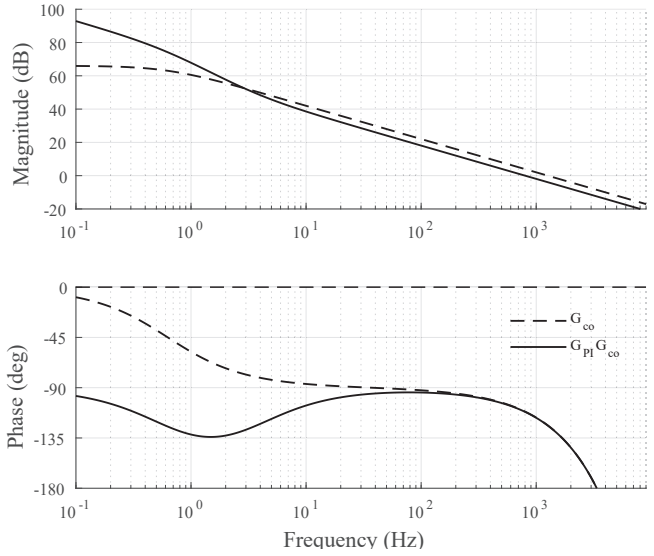

Fig. 5. Control to input transfer function (dashed line) and controller loop gain (solid line).

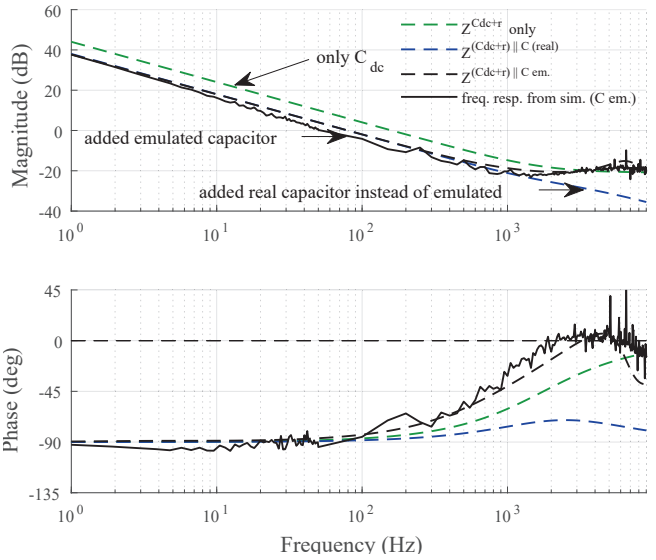

Fig. 6. Output impedance of emulated and real capacitors in parallel with dc-link capacitor.

was set in parallel with the dc-link. As expected, the addition of the capacitor decreases the magnitude similarly as in Fig. 1.

In the third case (dashed black line), the BESS was connected to the dc-link and set to emulate a capacitor (1 mF) instead of using the additional capacitor. This corresponds to the analysis in (11). The solid black line presents the corresponding frequency response obtained directly from MATLAB Simulink simulation model by using a nonparametric identification based on pseudo-random-binary-sequence (PRBS) injection and Fourier methods [13], [14]. The frequency response was obtained by inserting a controllable current source in parallel with the dc-link and injecting the PRBS perturbation with it. Note that the nominal output current was set to 0 A. As the figure shows, the derived output impedance of the emulated capacitor follows the measured impedance highly accurately in a wide frequency band.

With an ideal controller, the impedance with the capacitor emulation would equal to the case with the additional capacitor. However, the accuracy of the emulation depends on the controller performance; e.g, the cross-over frequency of the current controller. To demonstrate the effect of the controller cross-over frequency, Fig. 7 presents the output impedance in the case of a controller with a) 800 Hz (black solid line) and b) 500 Hz (green solid line) crossover frequency. With the higher crossover frequency, the magnitude of the emulated output impedance follows the output impedance of the additional capacitor up to higher frequencies due to the faster controller. However, the difference between them is small since the crossover frequencies are not significantly different.

To verify the correct operation of the control algorithm, a grid-connected battery-PV system illustrated in Fig. 8 was simulated under grid imbalance with and without the capacitance emulation. The imbalance is simulated by setting phase

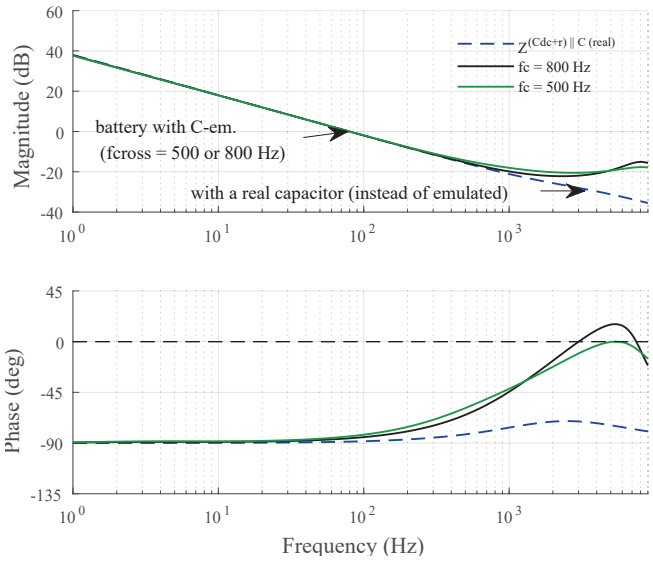

Fig. 7. The output impedance of emulated capacitor in parallel with the dc-link capacitor with different controller crossover frequencies.

A voltage magnitude to 70 %. This introduces a second order harmonic component to the dc-link voltage, as can be seen in Fig. 9, which presents the dc-link voltage when the capacitor emulation is set at 25 ms. As a result, the second harmonic component decreases from 0.24 % to 0.13 % and the total harmonic distortion (THD) from 0.31 % to 0.24 %. Hence, it is clear that the second harmonic mitigation is successful as it is within the controller bandwidth.

Furthermore, since the battery charger controls the current in an oscillatory manner such that it mitigates the second harmonic component of the dc-link voltage, the current drawn

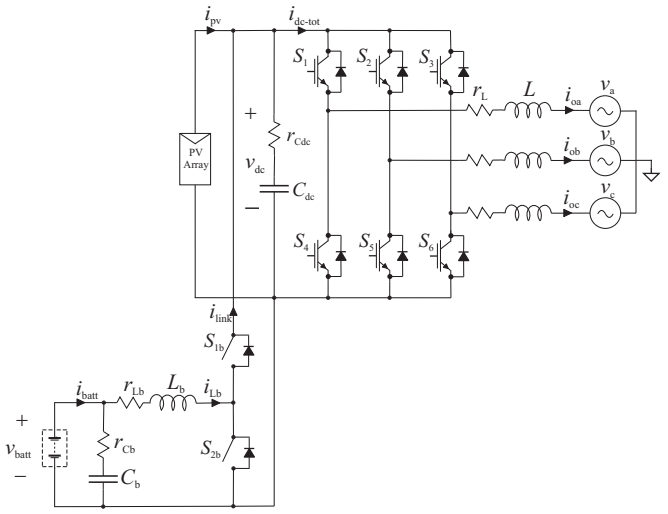

Fig. 8. The battery charger (bi-directional dc-dc converter) connected to a PV inverter.

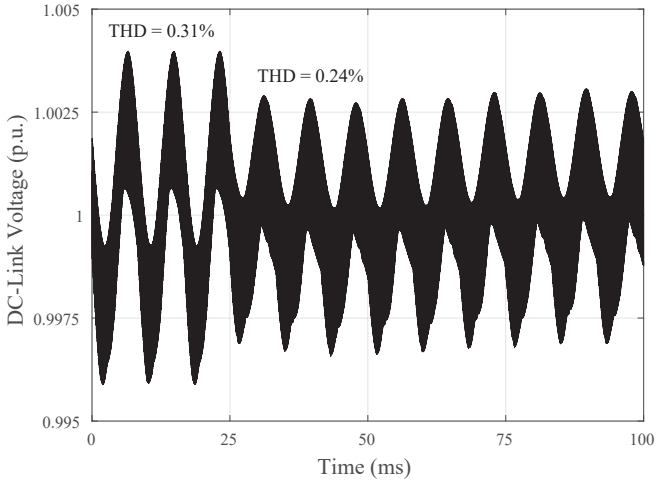

Fig. 9. Simulated dc-link voltage during grid imbalance; grid voltage phase A amplitude is set to 70 %. The capacitor emulation algorithm is set on at 25 ms.

from the battery is relatively low and periodical in the sense that the average current remains at 0 A. Hence, the control scheme does not require a large battery and the state of charge (SOC) of the battery remains constant except for internal losses. However, it should be noted that the battery SOC is still a limiting factor for the correct operation of the control algorithm, as the battery should not be allowed to over- or undercharge.

V. Conclusion

This paper has studied a method to control a BESS to emulate a capacitor so that the dc-link voltage fluctuation can be mitigated. The analysis and simulation results demonstrate that the battery can be controlled to emulate a capacitance within the battery charger's control bandwidth. As a result, the system dynamics can be adjusted by using this controllable virtual capacitance.

The analysis was performed using small-signal models to enable reliable and straightforward investigation of the system dynamics for control design. The derived model can also be used to initiate stability analysis at the output of a battery charger, e.g. at the dc-link. The analysis was confirmed by simulations both in the time and frequency domain. However, it is emphasized that the battery SOC is a limiting factor for the correct operation of the control algorithm. Furthermore, the battery should not be allowed to over- or undercharge to guarantee safety and reliability of the system.

Controlling the battery to emulate a capacitor can be highly efficient, for example, if an inverter connected to the dc-link is operating under heavily imbalanced grid conditions and the dc-link capacitor is not enough to suppress the voltage fluctuation. The same effect can be achieved by increasing the dc-link capacitance. Depending on the application, the control scheme could also allow a reduced capacitance being used. However, as the control algorithm changes the system dynamics, the desired operation of the inverter must be ensured.

Appendix

The state, input, output, and feed-through matrices used in (7) are defined as

$$\mathbf{A} = \begin{bmatrix} -\dfrac{1}{C_\mathrm{b} r_\mathrm{Cb}} & 0 \\ 0 & \dfrac{R_\mathrm{eq1}}{L_\mathrm{b}} \end{bmatrix}, \; \mathbf{B} = \begin{bmatrix} \dfrac{1}{C_\mathrm{b} r_\mathrm{Cb}} & 0 & 0 \\ \dfrac{1}{L_\mathrm{b}} & \dfrac{D-1}{L_\mathrm{b}} & \dfrac{V_\mathrm{eq}}{L_b R_\mathrm{eq2}} \end{bmatrix},$$
$$\mathbf{C} = \begin{bmatrix} -\dfrac{1}{r_\mathrm{Cb}} & 1 \\ 0 & 1-D \end{bmatrix}, \quad \mathbf{D} = \begin{bmatrix} \dfrac{1}{r_\mathrm{Cb}} & 0 & 0 \\ 0 & 0 & -\dfrac{V_\mathrm{batt}+(D-1)V_\mathrm{link}}{R_\mathrm{eq2}} \end{bmatrix}, \tag{14}$$

respectively, where

$$\begin{aligned} R_\mathrm{eq1} &= (r_\mathrm{Lb} + r_\mathrm{sw1})\,(D-1) - D\,(r_\mathrm{Lb} + r_\mathrm{sw2})\,, \\ R_\mathrm{eq2} &= r_\mathrm{Lb} + r_\mathrm{sw1} + D\,(r_\mathrm{sw2} - r_\mathrm{sw1})\,, \\ V_\mathrm{eq} &= (r_\mathrm{Lb} + r_\mathrm{sw2})V_\mathrm{link} + (r_\mathrm{sw1} - r_\mathrm{sw2})V_\mathrm{batt}, \end{aligned} \tag{15}$$

r_sw1 is the internal on-time resistance of the switch S_1 and r_sw2 the internal on-time resistance of the switch S_2 and the rest of the variables are as given in Fig. 2. Furthermore, the capital letters represent steady-state values and the steady-state value of the duty cycle is defined as in Eq. 16.

$$D = \frac{V_\mathrm{link} - V_\mathrm{batt} + I_\mathrm{batt}^\mathrm{ref}\,(r_\mathrm{Lb} + r_\mathrm{sw1})}{V_\mathrm{link} + I_\mathrm{batt}^\mathrm{ref}\,(r_\mathrm{sw1} + r_\mathrm{sw2})} \tag{16}$$

References

[1] IRENA, *Electricity Storage and Renewables: Costs and Markets to 2030*. International Renewable Energy Agency, 2017.

[2] E. Telaretti and L. Dusonchet, "Battery storage systems for peak load shaving applications: Part 1: Operating strategy and modification of the power diagram," in *2016 IEEE 16th International Conference on Environment and Electrical Engineering (EEEIC)*, June 2016, pp. 1–6.

[3] R. Hidalgo-Len, D. Siguenza, C. Sanchez, J. Len, P. Jcome-Ruiz, J. Wu, and D. Ortiz, "A survey of battery energy storage system (bess), applications and environmental impacts in power systems," in *2017 IEEE Second Ecuador Technical Chapters Meeting (ETCM)*, Oct 2017, pp. 1–6.

[4] Y. Tian, A. Bera, M. Benidris, and J. Mitra, "Stacked revenue and technical benefits of a grid-connected energy storage system," *IEEE Transactions on Industry Applications*, vol. 54, no. 4, pp. 3034–3043, July 2018.

[5] H. Wang and F. Blaabjerg, "Reliability of capacitors for dc-link applications in power electronic convertersan overview," *IEEE Transactions on Industry Applications*, vol. 50, no. 5, pp. 3569–3578, Sep. 2014.

[6] W. Lee and S. Sul, "Dc-link voltage stabilization for reduced dc-link capacitor inverter," *IEEE Transactions on Industry Applications*, vol. 50, no. 1, pp. 404–414, Jan 2014.

[7] C. Ren, X. Han, L. Wang, Y. Yang, W. Qin, and P. Wang, "High-performance three-phase pwm converter with a reduced dc-link capacitor under unbalanced ac voltage conditions," *IEEE Transactions on Industrial Electronics*, vol. 65, no. 2, pp. 1041–1050, Feb 2018.

[8] D. Bazargan, B. Bahrani, and S. Filizadeh, "Reduced capacitance battery storage dc-link voltage regulation and dynamic improvement using a feedforward control strategy," *IEEE Transactions on Energy Conversion*, vol. 33, no. 4, pp. 1659–1668, Dec 2018.

[9] E. Afshari, G. R. Moradi, R. Rahimi, B. Farhangi, Y. Yang, F. Blaabjerg, and S. Farhangi, "Control strategy for three-phase grid-connected pv inverters enabling current limitation under unbalanced faults," *IEEE Transactions on Industrial Electronics*, vol. 64, no. 11, pp. 8908–8918, Nov 2017.

[10] E. Shoubaki, S. Essakiappan, M. Manjrekar, and J. Enslin, "Synthetic inertia for bess integrated on the dc-link of grid-tied pv inverters," in *2017 IEEE 8th International Symposium on Power Electronics for Distributed Generation Systems (PEDG)*, April 2017, pp. 1–5.

[11] S. Chakraverty, N. Mahato, P. Karunakar, and T. Dilleswar Rao, *Advanced Numerical and Semi-Analytical Methods for Differential Equations*. Wiley, 2019.

[12] H. H. Rosenbrock, *State-Space and Multivariable Theory*. Nelson, 1970.

[13] J. Schoukens, K. Godfrey, and M. Schoukens, "Nonparametric data-driven modeling of linear systems: Estimating the frequency response and impulse response function," *IEEE Control Systems Magazine*, vol. 38, no. 4, pp. 49–88, Aug 2018.

[14] T. Roinila, J. Huusari, and M. Vilkko, "On frequency-response measurements of power-electronic systems applying mimo identification techniques," *IEEE Transactions on Industrial Electronics*, vol. 60, no. 11, pp. 5270–5276, Nov 2013.